Uludağ University Journal of The Faculty of Engineering, Vol. 31, No. 1, 2026 RESEARCH

DOI: 10.17482/uumfd.1737606

SIZE EFFECTIVE MODAL BEHAVIOR OF STRETCHABLE E-SKIN FOR HUMANOID ROBOTS AND PROSTHETIC HAND

Kadir MERCAN *

Received: 08.07.2025; revised: 30.09.2025; accepted: 15.12.2025

Abstract: As sensor technology advances, the dimensions of components continue to shrink to the nanoscale, making the consideration of size effects imperative for accurate design and analysis. This study investigates the modal behavior of stretchable electronic skin (e-skin) for humanoid robots and prosthetic hands, explicitly accounting for the micro-nanoscale effects of the sensor layer. While molecular dynamics simulations with tools like LAMMPS provide realistic results by incorporating atomic interactions, they are computationally prohibitive for systems of micrometer dimensions, which can contain over 3.8×10^{11}-5×10^{11} atoms. To bridge this scale gap, molecular dynamics simulations were employed to calibrate the nonlocal parameter (e_0a) of the Eringen nonlocal elasticity theory for graphene, graphene oxide (GO), and reduced graphene oxide (rGO) nanosensors on a SiO_2 substrate. These calibrated parameters were then integrated into ANSYS and COMSOL Multiphysics, finite element software that typically does not incorporate nanoscale effects. A comparative modal analysis was performed using classical plate theory, standard finite element methods, and the proposed size effect considered finite element approach. Realistic boundary conditions modeling the sensor's connection to an electronic circuit were applied. The results demonstrate that employing realistic boundary conditions, as opposed to idealized clamped supports, leads to a significant reduction in natural frequencies by an average of 43%, underscoring the critical importance of accurate modeling for predictive design.

Keywords: Atomic simulation, Humanoid robot, Prosthetic hand, Frequency, Graphene-GO-rGO, Nonlocal F.E.A.

İnsansı robotlar ve protez ellerde esneyebilir yapay derinin boyut etkili modal davranışı

Öz: Sensör teknolojisindeki ilerlemeyle bileşen boyutları nanometre ölçeğine doğru küçülmekte ve bu da hassas tasarım ve analiz için boyut etkilerinin dikkate alınmasını zorunlu kılmaktadır. Bu çalışma, insansı robotlar ve protez eller için esneyebilir elektronik deri (e-skin) modüllerinin modal davranışını, sensör nano tabakasının boyut etkileri açıkça modellenerek incelemektedir. LAMMPS gibi araçlarla yapılan moleküler dinamik simülasyonlar atomik etkileşimleri içerdiği için gerçekçi sonuçlar verse de, 3.8×10^{11}-5×10^{11}atom içerebilen mikrometre boyutlarındaki sistemler için hesaplama açısından uygulanabilir değildir. Bu ölçek boşluğunu kapatmak için, bir SiO_2 substratı üzerindeki grafen, grafen oksit (GO) ve indirgenmiş grafen oksit (rGO) nanosensörlerinin Eringen yerel olmayan elastisite teorisinin parametresi (e_0a) olan boyut sabiti, moleküler dinamik simülasyonlarla hesaplanmıştır. Kalibre edilen bu parametreler, normalde nano ölçek etkilerini içermeyen sonlu elemanlar yazılımları ANSYS ve COMSOL Multiphysics'e entegre edilmiştir. Karşılaştırmalı bir modal analiz, klasik plak teorisi, standart sonlu elemanlar yöntemleri ve önerilen boyut etkili sonlu elemanlar yaklaşımı kullanılarak gerçekleştirilmiştir. Sensörün elektronik bir devreye bağlantısını modelleyen gerçekçi sınır koşulları uygulanmıştır. Sonuçlar, idealize edilmiş ankastre mesnet modellemesi yerine gerçekçi sınır koşullarının kullanılmasının, doğal frekanslarda ortalama %43'lük önemli bir azalmaya yol açtığını göstermekte ve tahminsel tasarım için doğru modellemenin kritik önemini vurgulamaktadır.

Anahtar Kelimeler: Atomik simülasyon, İnsansı robot, Protez el, Frekans, Grafen-GO-rGO

---

* Burdur Mehmet Akif Ersoy University, Civil Engineering Department, 15030, Burdur, Türkiye.
Corresponding Author: Kadir Mercan (kmercan@mehmetakif.edu.tr)

1. INTRODUCTION

First ideas, steps and basic designs of humanoid robots started in early 70s. The physical evolution of humanoid robots began Waseda University's WABOT project. WABOT-1 (1973) was the first humanoid robot capable of balancing on two legs and grasping simple objects (Kato, 1973; Kato et al., 1987). During this period, robots were heavy, cumbersome, and slow due to the limitations of motor technology. Honda's E series, launched in 1986, focused on developing walking mechanisms and achieved dynamic walking with the P2 robot in 1996 (Hirai et al., 1998). This design laid the foundation for today's humanoid robots. In the 2000s, ASIMO (2000) popularized humanoid robot technology. Weighing 57 kg, this robot could run at 6 km/h and climb stairs (Hirose and Ogawa, 2007). However, expensive hydraulic systems and energy consumption were significant limitations. Concurrently, Boston Dynamics developed PETMAN, a military-purpose prototype that mimicked biomechanical human movements (Nelson et al., 2012). During this period, carbon fiber body designs and DC servo motors became widespread.

The suitability of graphene's mechanical properties for e-skin applications was first demonstrated at the University of Manchester (Castro Neto et al., 2009; Li et al., 2009). In 2010, the first flexible pressure sensor was produced using the water solubility of graphene oxide (GO) (Kim et al. 2009, Suk et al., 2010). In 2011, the University of Tokyo developed sensors capable of operating at 95% humidity by demonstrating the biocompatibility of GO (Wang et al., 2011). In 2014, researchers from Cambridge produced an ultra-thin e-skin with a thickness of 50 nm using GO's self-assembly property (Gao et al., 2023).

The integration of graphene into electronic skin (e-skin) systems has gained significant momentum over the past fifteen years, in line with the rise of nanomaterials science. First isolated in 2004, graphene has attracted attention due to its two-dimensional carbon structure with a thickness of a single atom, and has become a leading material in e-skin applications, particularly due to its properties such as mechanical flexibility, electrical conductivity, and chemical resistance (Mercan, 2009). Since the early 2010s, research has focused on graphene's piezoresistive properties, aiming to develop sensor platforms capable of detecting various sensory signals such as touch, pressure, temperature, and humidity. In the 2020s, graphene has been combined with different to enhance its mechanical flexibility and diversify its functional properties. During this process, multifunctional e-skin prototypes such as piezoresistive sensors, piezocapacitive layers, and temperature sensors were produced (Li et al., 2025). Additionally, sensor sensitivity and linear sensing ranges have been expanded through micro-nano structures, accelerating the application of graphene e-skins in medical monitoring, human-machine interfaces, and robotic skin systems. A comprehensive review study conducted by Liu and Liu (2025) summarized the physical and chemical advantages of graphene in flexible sensors. The study details how graphene and its derivatives (such as GO and rGO) play a critical role in pressure, temperature, humidity, and biosensor applications due to their superior electrical conductivity, mechanical flexibility, and chemical stability. The potential of these sensors in areas such as wearable devices, e-skin, health monitoring, and environmental monitoring is also highlighted. The authors comparatively studied various sensor types based on parameters such as fabrication methods, flexibility/mechanical strength relationship, signal response times, and long-term stability, and revealed that graphene-based materials are one of the most promising materials for next-generation sensors due to their high sensitivity and multi-sensing capabilities.

2. E-SKIN: GRAPHENE, GRAPHENE OXIDE AND REDUCED GRAPHENE OXIDE

GO and rGO are chemically modified forms of graphene. These materials exhibit different mechanical and dynamic properties due to oxygen-containing functional groups (Dikin et al., 2007). GO has a higher damping capacity than graphene, making it suitable for vibration damping applications (Lee et al., 2011). However, rGO's partially reduced structure increases electrical conductivity while also altering its mechanical properties. Understanding the dynamic behavior of these materials plays a critical role in applications such as flexible electronics and biomedical sensors (Eda and Chhowalla, 2010).

Graphene, GO, and rGO are important representatives of carbon-based nanomaterials and offer unique advantages in flexible electronics and, in particular, electronic skin (e-skin) applications (Geim and Novoselov, 2007; Zhu et al., 2010). The fundamental differences between these three forms stem from their atomic-level structural properties, which directly influence the materials' electrical, mechanical, and chemical behavior (Pei and Cheng, 2012).

Graphene exhibits a two-dimensional structure consisting of pure sp^2 hybridized carbon atoms arranged in a hexagonal (hexagonal) pattern. Graphene produced by chemical vapor deposition (CVD) is the most commonly used method for producing high-quality, large-area films (Li et al., 2009). In contrast, GO is obtained by treating graphene with strong oxidizing agents (Hummers method) and contains oxygen-containing functional groups such as hydroxyl, epoxy, and carboxyl groups in its structure (Dreyer et al., 2010). rGO, on the other hand, is produced by the chemical, thermal, or photochemical reduction of GO and possesses a partially restored sp^2 carbon network (Zhu et al., 2010). During the reduction process, a large portion of the oxygen functional groups in GO are removed, but some defects and functional groups remain in the structure (Pei and Cheng, 2012).

Graphene is one of the strongest materials known, with a Young's modulus of 1 TPa and a tensile strength of 130 GPa (Lee et al., 2008; Civalek et al., 2021). These properties make it ideal for e-skin applications that require mechanical durability and flexibility (Lipomi et al., 2011). In contrast, the mechanical properties of GO are quite low (Young's modulus ≈200–500 GPa) (Suk et al., 2010). However, GO is suitable for solution-based production techniques due to its water solubility and ease of processing (Dikin et al., 2007). rGO occupies a position between graphene and GO in terms of mechanical properties (Young's modulus ≈0.3–0.8 TPa) (Chen et al., 2020). With these properties, rGO stands out as a material that offers both sufficient mechanical strength and processability. Structures of graphene, GO, and rGO are demonstrated in Figure 1 respectively.

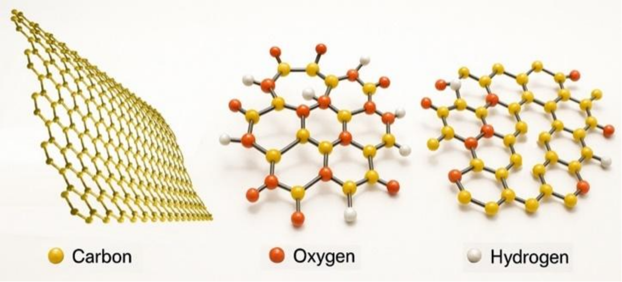

Figure 1:
Nanostructures of Graphene, GO, rGO

Electronic skin (e-skin) is an artificial sensor system that mimics the functions of human skin and has the potential to provide a realistic sense of touch, particularly in humanoid robots and prosthetic hand systems. In modern e-skins, the goal is for tactile perception to detect not only pressure but also multimodal stimuli such as temperature, humidity, texture, hardness, proximity, and vibration. Thanks to TVAN-SPAN neuron-like sensors developed as “zero-biased” types, it is possible to characterize contact within a range of surface roughness (0.8–1600 µm) and hardness (6HA–85HD) (Guo et al., 2024). With deep learning techniques, these tactile data can be both classified and interpreted (Mu et al., 2024). Additionally, new-generation e-skins have developed bidirectional systems that can provide both touch perception and vibrational feedback wirelessly (Li et al., 2022). Very recently, Min et al. (2025) demonstrated a flexible touch sensor with deep learning-supported 3D force analysis capabilities has been developed for human-robot interfaces. The sensor can accurately detect multi-axis pressure and tensile forces and convert this data into three-dimensional force vectors using a deep learning model. This work represents a significant step toward developing realistic touch sensation and object manipulation, particularly in prosthetic hands and humanoid robots. These systems enable the wireless transmission of touch data from one user to another, opening new horizons for education, healthcare, and social communication applications. Especially in prosthetic applications, e-skins that mimic the functions of mechanoreceptors (Merkel, Ruffini, Pacinian, Meissner) with biomimetic sensor systems can produce neuromorphic data by integrating with the nervous system, thereby enabling the neural transmission of touch sensation (Iskarous and Thakor, 2019; Wang et al., 2023).

Table 1. Comparative Material Properties of Graphene, GO, and rGO <(Suk et al., 2010; Eda et al., 2008; He et al., 2024; Liu et al., 2025)>

	Graphene	GO	rGO
Chemical Structure	Pure sp^2 carbon web	Oxygen-containing functional groups	Partial sp^2 restoration
Production Method	C.V.D.	Hummers Method	Thermal reduction
Layer Thickness	0.34 nm	0.7-1.2 nm	0.5-0.8 nm
Young's Modulus	1 TPa	200-500 GPa	300-800 GPa
Poisson Ratio	0.165	0.21	0.18
Tensile Strength	130 GPa	10-50 GPa	50-100 GPa
Thermal Conductivity	5000 W/mK	1-10 W/mK	100-1500 W/mK
Electrical Conductivity	10^8 S/m	10^{-2}-10^2 S/m	10^3-10^5 S/m (
Band Gape	0 eV	1.7-2.4 eV	0.1-0.9 eV
Pressure Sensitivity	0.05 Pa	1 Pa	0.5 Pa
Responce Time	<0.2 ms	10-100 ms	1-10 ms
Stable Temperature	-200°C 400°C	-50°C 150°C	-100°C 300°C
Abrasion Resistance	100,000+ cycle	10,000 cycle	50,000 cycle

As it can be clearly seen in Figure 1-2 and Table 1, graphene is a two-dimensional structure composed of pure sp^2 hybridized carbon atoms arranged in a hexagonal (hexagonal) pattern and is typically produced using the chemical vapor deposition (CVD) method. This method is the most commonly used technique for obtaining high-quality and large-scale graphene films (Geim and Novoselov, 2007). GO, on the other hand, is obtained by treating graphene with strong oxidizing agents (Hummers method) and contains oxygen-containing functional groups such as hydroxyl, epoxy, and carboxyl (Dreyer et al., 2010). RGO is produced by the chemical or thermal reduction of GO and has a partially restored sp^2 carbon network (Pei and Cheng, 2012). This reduction process removes a large portion of the oxygen functional groups in GO while leaving some defects and functional groups in the structure. Comparing physical and mechanical properties, Graphene is one of the strongest materials known, with a Young's modulus of 1 TPa and a tensile strength of 130 GPa (Lee et al., 2008, Mercan et al., 2017; Arefi et al., 2021). These properties make graphene ideal for e-skin applications that require mechanical durability and flexibility. In contrast, the mechanical properties of GO are significantly lower (Young's modulus ≈200–500 GPa) (Suk et al., 2010).

3. HUMANOID ROBOTS AND PROESTETICS

In recent years, the use of graphene-based materials in artificial prosthesis technologies has made significant progress. Wang et al. (2020) documented that rGO/polydimethylsiloxane

(PDMS) composites exhibited 50000 cycles of stability under 300% strain and provided 5 Pa pressure sensitivity. These materials have been used for tactile feedback in prosthetic fingertips and have demonstrated performance close to that of human skin with a response time of 10 ms. Zhang et al. (2022) designed hybrid structures containing free-standing rGO electrodes directly patterned by laser to develop wearable capacitive pressure sensors. Complementary helical microstructures integrated into the tethered band enabled the development of sensors offering dual-mode (pressure and proximity) sensing. While showing high sensitivity in the measurement range of 0-14 kPa (on the order of kPa-^{1}), the possibilities for real-time monitoring of finger movements and applications in wearable electronics have been validated. The results show that this method is a simple, fast and efficient solution for producing high performance sensors.

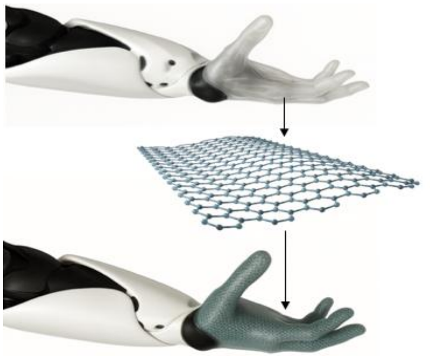

Figure 2:
Nanomaterials on Robotic-Prosthetic hand

The application of sensing layer at robotic or prosthetic hand is demonstrated in Fig. (2). Covering the entire hand inside-out with a sensor layer would result in very high sensing and stability. However, the high production costs and the limited long-term biodegradation data have been identified as significant barriers (Al-Daraghmeh, 2023). Therefore, it would be more reasonable and feasible to apply the sensor coating only to the areas of the hands that need to sense (palms and fingers). As shown in Figure 2, the regions where graphene, GO, or rGO coatings on a humanoid robot or prosthetic hand would be effective and more cost-efficient are demonstrated. It is also shown that one side of the sensor layer in contact with the outer surface is exposed, while the other side is in contact with the inner surface of the robotic hand. In this study, the two-variable Winkler-Pasternak surface modeling was utilized for the mathematical modeling of this sensor layer based on continuous medium mechanics.

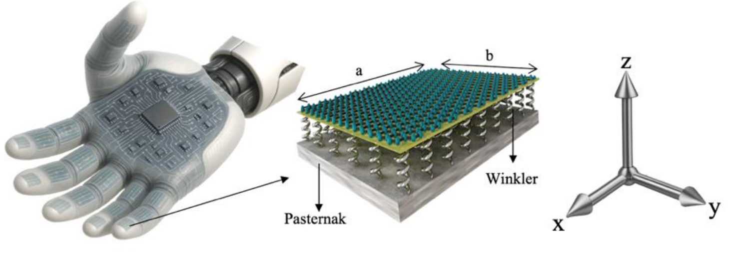

Figure 3:
Details of Coating Nanomaterials on Robotic-Prosthetic Hand and its Continuum Model

GO-based bionic applications have also shown remarkable developments in recent years. In a comprehensive survey Jyothish and Mishra (2024) systematically analyzed the evolution of robotic prosthetics over the last 15 years, specifically in the context of neuroprostheses, soft actuators and control strategies. In the review, neuromorphic sensor interfaces and brain-machine interface technologies are evaluated with longitudinal performance metrics, detailing advances in cross-channel audibility and the sensitivity and latency characteristics of brainless applications. Soft actuator architectures are categorized into elastomer, piezoelectric and magnetic actuation systems and their impact on biomimetic motion simulation and user adaptation processes are explained. In the control strategies section, model-based adaptive control methods, machine-learned motor commands and offline/online feedback algorithms are compared, and it is emphasized that calibration processes, especially with deep learning, increase the naturalness of prosthetic responses. It is also noted that hardware-software integration is critical in terms of modularity, power consumption, cost, and safety, and pointed out that hybrid systems focusing on sensor fusion and real-time analysis of human-brain signals should be developed for future research. Complementing this, Zhang et al. (2025) presented an AI-enhanced framework for processing tactile data from prosthetic skins, significantly improving pattern recognition and response times.

4. MODAL ANALYSES: EXACT SOLUTION, NANOSCALED COMSOL AND ANSYS

Modal analysis is one of the cornerstones of structural dynamics and is used to determine the natural frequencies, mode shapes, and damping characteristics of materials (Mercan et al., 2018; 2020). This analysis method is widely used in engineering and materials science to understand the dynamic responses of structures, provide vibration control, and minimize resonance risks (Ewins, 2009; Mercan et al., 2016; Demir et al., 2017). Numerical simulation tools such as MATLAB, COMSOL Multiphysics, and ANSYS are widely used in this field since many years (Maia and Silva, 1997; Numanoğlu et al., 2017; Geetha et al., 2025). MATLAB offers an effective solution, particularly for small and medium-scale problems due to matrix-based calculations and its ability to develop customizable algorithms (Khorasani et al., 2021; Mukherjee et al., 2021). COMSOL Multiphysics stands out in the analysis of complex systems due to its ability to simulate multiple physical phenomena in an integrated manner and its user-friendly interface (Mercan, 2019). ANSYS, on the other hand, is preferred for the analysis of large-scale models due to its high computational performance and widespread use in industrial applications (Mercan and Civalek, 2022). Recent studies have shown that these software programs have been successfully applied in a wide range of fields, from graphene-based nanoelectromechanical systems to flexible electronics and aerodynamic structures (Gunes et al., 2025).

Understanding the dynamic behavior of two-dimensional (2D) materials such as graphene, GO, and rGO is of critical importance for advanced technology applications such as flexible electronics, biosensors, artificial skin (e-skin), and high-frequency nanoelectromechanical systems (NEMS). In recent years, the experimental and numerical investigation of the vibrational characteristics of these materials has become an important research topic in materials science and structural mechanics (Thang et al., 2025).

CCCC (four side clamped) modeling is an ideal engineering abstraction. In reality, no system is perfectly embedded. Especially in nanoelectronic applications, edge effects, adhesion problems, and directed charges increase the necessity of circuit-connected modeling. Circuit-connected boundary conditions are situations where nano plates are electrically and physically fixed either directly to the PCB surface, to silicon oxide layers, or via metal conductive pads. Metal pads, solder joints, or adhesive layers placed on the edges of nano plates are close to a fully embedded (clamped) condition but are not completely rigid. Therefore, this fixation is modeled by restricting both displacement and rotational degrees of freedom at the edges (Ciuprina, 2022).

Electric Circuit Element (ECE) boundary conditions are applied to sensing graphene, GO, and rGO elements fixed to silicon oxide layer to obtain most realistic results in calculations. In this case ECE, provides a fully rigid connection with the sensor layer on the SiO_2-based adhesive.

$$\mathrm{w} = 0, \qquad \frac{\partial \mathrm{w}}{\partial \mathrm{n}} = 0 \tag{1}$$

Although w=0 is assumed in both CCCC and ECE cases, in circuit-connected models this assumption is only valid for contact regions. Under CCCC conditions, the vertical displacement at all edge nodes is zero. This condition ensures that the edges of the plate or shell do not deviate from the ground plane at any point (Ersoy et al., 2018). Similarly, in most cases, the vertical displacement at the edges of a structure resting on a surface such as SiO_2 is also assumed to be zero. However, this applies only to cases where there is complete mechanical contact and no delamination or slippage. The rotational degrees of freedom are also zeroed at the boundary conditions. In other words, the edges cannot bend and are completely fixed. In circuit-connected cases, instead of this absolute constraint, a moment resistance connected to the edges with elastic springs is applied:

$$M_n = -k_\theta \theta \tag{2}$$

Here, k_θ is the spring stiffness, the quality of contact determines this value. θ is edge slope. CCCC boundary conditions are a purely mechanical abstraction and do not include electrical interactions. In circuit-coupled modeling, however, the structure is usually in electrical contact with a metal pad, a SiO_2 surface, or a PCB trace. This contact directly transfers numerous effects, such as thermal expansion differences, electromigration, and dielectric boundary effects, to the vibration behavior (Ciuprina, 2021; Arefi et al., 2021). In terms of stiffness, CCCC boundary conditions provide maximum system stiffness because both rotation and displacement are limited at the edges (Mercan et al., 2016). These increases both mode shapes and frequencies. On the other hand, in structures placed on dielectric substrates such as SiO_2, stiffness depends on the physical properties of the contact (e.g., adhesion energy, pad size, edge stability) (Numanoğlu et al., 2019; Sobhani et al., 2022).

Classical modal analysis can be performed using Kirchoff plate theory, first Hamilton principle:

$$\delta \int_{t_1}^{t_2} \left(0.5 \int \rho h \left(\frac{\partial \omega}{\partial t} \right)^2 dA - 0.5 \int_V \sigma_{ij} \in_{ij} dV + \int \left(F_{el} + F_{th} \right) \omega dA \right) dt = 0 \tag{3}$$

$$F_{el} = \frac{\in_0 \in_\tau V^2}{2(d-w)^2} \qquad F_{th} = -Eh \propto \Delta T \nabla^2 \omega \tag{4}$$

$$D \nabla^4 \omega = \rho h \frac{\partial^2 \omega}{\partial t^2} \tag{5}$$

$$D = \frac{Eh^3}{12(1-v^2)} \tag{6}$$

Here D is bending rigidity (Civalek and Demir, 2011), E Young modulus, h thickness of sensing layer, v Poisson ratio, $\in_0$Vacuum permittivity, $\in_\tau$ relative dielectric constant, F_{el} and F_{th} electrostatic force, thermal strain respectively. Pull-in Voltage Formula and Moment Balance due to electronic circuit can be stated as:

$$V_{cr} = \sqrt{\frac{8Dd^3}{27 \in_0 L^4}} \qquad D \frac{\partial^2 \omega}{\partial n^2} \bigg|_{\partial \Omega} = -\frac{\in_0 V^2 L^2}{8d^2} - Eh \propto \Delta T + F_{con} \tag{8}$$

Where $\propto$ represent thermal expansion coefficient, F_{con} Circuit connection strength, V Voltage, d sensing layer-substrate distance, ΔT Temperature difference. The global balance in corner conditions:

$$\oint_{d\Omega}\left(\frac{\partial \omega}{\partial \mathrm{n}}-\frac{V^2L^2}{4D}\right)ds=0 \tag{9}$$

As sensing layers are in the nanoscale, to add the nonlocal size effect, place the stress expression in the energy equation and take the variation.

$$(1-\mu\nabla^2)(\mathrm{D}\nabla^4\omega)=\rho\mathrm{h}\frac{\partial^2\omega}{\partial t^2}-F_{ex} \tag{10}$$

F_{ex} expresses the total force components applied to a system from outside. Since the sensor layer is in contact with the electronic circuit in the palm and fingertips, the two-parameter Winkler-Pasternak foundation model is used to model the contact effect as follows (Akgöz et al., 2016; Demir et al., 2017) where k_W and k_P are Winkler base module (vertical spring stiffness) and Pasternak shear modulus (lateral stiffness) respectively (Mercan et al., 2015; 2019). In order to model electronic elements more realistic, to include electrostatic force:

$$F_{WP}=k_W\omega-k_P\nabla^2\omega \qquad\qquad F_{EF}=\nabla^2\omega \tag{11}$$

Dielectric effect varying with distance in electrostatic force:

$$\in_e=\in_0\in_\tau\left(1+\frac{\left(\frac{x}{L}+\frac{y}{L}\right)^2}{5}\right) \tag{12}$$

Combining Eqs. (1-11) final nonlocal equation which will be used for classical and size effective exact solutions combined with electrical forces can be obtained as:

$$(1-\mu\nabla^2)\mathrm{D}\nabla^4\omega+k_W\omega-k_P\nabla^2\omega+\frac{\in_0\in_\tau V^2}{2(d-w)^2}-Eh\propto\Delta T\nabla^2\omega=\rho\mathrm{h}\frac{\partial^2\omega}{\partial t^2} \tag{13}$$

To obtain weak form of differential equation Galerkin's method can be used as:

$$\begin{aligned}\int_\Omega \psi\left[(1-\mu\nabla^2)\mathrm{D}\nabla^4\omega+k_W\omega-k_P\nabla^2\omega+\frac{\in_0\in_\tau V^2}{2(d-w)^2}-Eh\propto\Delta T\nabla^2\omega\right]d\Omega \\ =\int_\Omega \psi\rho\mathrm{h}\frac{\partial^2\omega}{\partial t^2}d\Omega\end{aligned} \tag{14}$$

Partial Integration of Nonlocal Terms and Application of Green's Theorem

$$-\mu\int_\Omega \psi\nabla^2\mathrm{D}\nabla^4\omega d\Omega=\mu\int_\Omega \nabla\psi\nabla\mathrm{D}\nabla^4\omega d\Omega-\mu\oint_{d\Omega}\psi\frac{d}{\partial\mathrm{n}}\nabla\mathrm{D}\nabla^4\omega ds \tag{15}$$

$$\mu\int_\Omega \psi\nabla\mathrm{D}\nabla^4\omega d\Omega=-\mu\int_\Omega \nabla^2\psi\nabla\mathrm{D}\nabla^4\omega d\Omega+\mu\oint_{d\Omega}\psi n\nabla\mathrm{D}\nabla^4\omega ds \tag{16}$$

If all steps are combined, the resulting weak form terms are obtained as:

$$-\mu\int_{\Omega}\psi\nabla^2\mathrm{D}\nabla^4\omega d\Omega=\mu\int_{\Omega}\nabla^2\psi\mathrm{D}\nabla^4\omega d\Omega-\mu\oint_{d\Omega}\psi\frac{d}{\partial\mathrm{n}}\mathrm{D}\nabla^4\omega ds\nabla\psi n\mathrm{D}\nabla^4\omega \tag{17}$$

Implementing boundary conditions:

$$-\mu\mathrm{D}\oint_{d\Omega}\left(\psi\frac{\partial(\nabla^2\omega)}{\partial n}-\frac{\partial\psi}{\partial n}\nabla^2\omega\right)ds \tag{18}$$

Where $\frac{\partial(\nabla^2\omega)}{\partial n}$ represent edge moment gradient and $\nabla^2\omega$ the curvature. The expansion of the final weak form equation:

$$\begin{aligned}\int_{\Omega}\left(\psi\rho\mathrm{h}\frac{\partial^2\omega}{\partial t^2}+\nabla^2\psi\mathrm{D}\nabla^2\omega+\mu\nabla^2\psi\mathrm{D}\nabla^4\omega\right)d\Omega\\ =\int_{\Omega}F_{ex}\psi d\Omega+\oint_{d\Omega}\left(D\frac{\partial\psi}{\partial n}\nabla^2\omega-\psi\left(D\frac{\partial(\nabla^2\omega)}{\partial n}+k_P\frac{\partial\omega}{\partial n}\right)\right)ds\end{aligned} \tag{19}$$

The effect of electrostatic, thermal, and foundation reaction forces as distributed loads:

$$\int_{\Omega}F_{ex}\psi d\Omega=\int_{\Omega}\psi\left(\frac{\epsilon_0\epsilon_\tau V^2}{2(d-w)^2}d\Omega-Eh\propto\Delta T\nabla^2\omega+k_W\omega-k_P\nabla^2\omega\right)d\Omega \tag{20}$$

Moment Balance for the interaction between the curvature at the edge of the plate and the normal derivative of the test function with Circuit-Connected Conditions and nonlocal moment respectively

$$\oint_{d\Omega}D\frac{\partial\psi}{\partial n}\nabla^2\omega\,ds \tag{21}$$

$$-\oint_{d\Omega}\psi\left(D\frac{\partial(\nabla^2\omega)}{\partial n}+k_P\frac{\partial\omega}{\partial n}\right)ds \tag{22}$$

$$\mathrm{D}\left.\frac{\partial(\nabla^2\omega)}{\partial n}\right|_{\partial\Omega}=-\frac{\epsilon_0\,V^2L^2}{8d^2}-Eh\propto\Delta T+F_{con} \tag{23}$$

Molecular dynamics simulations play a critical role in determining the mechanical properties of nanoscale materials (Mercan and Civalek, 2022; 2023). In this study, the e_0a values, which are the fundamental parameters of the Eringen nonlocal elasticity theory (Civalek el al., 2009), were calculated for graphene, GO, and rGO using the open-source LAMMPS (Large-scale Atomic/Molecular Massively Parallel Simulator) software. The graphene model was created using the AIREBO (Adaptive Intermolecular Reactive Empirical Bond Order) potential function, which is highly suitable for simulating covalent carbon systems as it accurately captures the mechanics of sp^2 hybridization, bond breaking, and formation. For the GO model, which involves carbon, oxygen, and hydrogen interactions, the ReaxFF (Reactive Force Field) potential was used. ReaxFF is designed for reactive systems and effectively models the dynamics of oxygen-containing functional groups and their interactions with the carbon lattice. The rGO model was also simulated using ReaxFF to maintain consistency in describing the partial reduction process. The rGO model was modeled as a partially reduced form of GO with an oxygen/carbon ratio of approximately 12%. All simulations were performed at 300 K (NVT ensemble), with a time step of 0.5 fs and a total simulation time of 500 ps under periodic boundary conditions. To calculate the e_0a parameter, the system was first thermally equilibrated. At this stage, the system was equilibrated at 300 K using the “fix nvt” command, and 100,000 time steps were run. Then, deformation was applied to the system to obtain stress-strain data. A strain rate of 0.01% was applied in the x-direction using the “fix deform” command, and the stress values were recorded in the “stress_strain.dat” file. These data were fitted to the fundamental equation of the Eringen nonlocal theory to determine the e_0a parameter. The nonlocal model defines the relationship between stress and strain as $\sigma - (e_0a)^2\nabla^2\sigma = C\varepsilon$, where C represents the elasticity tensor (Mercan and Civalek, 2016; 2017). The nonlocal model was fitted to the stress-strain curve using the “curve_fit” function in Python, and the e_0a value was calculated. As a result of the simulations, the e_0a value for graphene was determined to be 0.35 nm (±0.02), for GO 0.52 nm (±0.03), and for rGO 0.41 nm (±0.02). Various validation studies were conducted to confirm the accuracy of these results. When the potential function effect was examined, it was found that there was less than a 5% difference between the AIREBO and ReaxFF potentials. Furthermore, when compared with atomic force microscopy (AFM) measurements in the literature, the values were found to be consistent with those in the range of 0.32–0.38 nm for graphene, 0.49–0.55 nm for GO, and 0.39–0.43 nm for rGO (Weiss, 2025).

The static and dynamic analysis of 100 μm × 100 μm monolayers of graphene, GO and rGO poses significant computational challenges in molecular dynamics simulations. For pure graphene, this macroscopic size corresponds to approximately 3.8×10^{11} carbon atoms based on a bond length of 1.42 Å and a unit cell area of 5.24 Å^2 containing two atoms. The presence of oxygen functional groups in GO and residual defects in rGO increases the total number of atoms by 10-30% to $4.2\text{-}5 \times 10^{11}$ atoms.

5. NUMERICAL RESULTS

Graphene and graphene-based materials (specifically, GO and rGO) have become increasingly important in nanoelectromechanical systems (NEMS) and flexible electronics applications in recent years. The primary objective of this study is to investigate the dynamic behavior of these materials under different aspect ratios (a/b = 1.0–2.0) with realistic boundary conditions, and to evaluate the effects of nonlocal effects and electronic circuit support on modal properties. As the mechanical behavior of nanoscale materials exhibits size-dependent effects that cannot be fully explained by classical continuum mechanics theories. The Eringen nonlocal elasticity theory was developed to overcome this limitation and is based on the assumption that material properties are related to long-range interatomic interactions. This theory is particularly important in the analysis of two-dimensional materials such as graphene, which are only one atom thick. In this study, the nonlocal parameter (e_0a) was calculated using LAMMPS molecular dynamics simulations and determined to be 0.35 nm, 0.52 nm, and 0.41 nm for graphene, GO, and rGO, respectively. These values were used in finite element analysis software such as ANSYS and COMSOL to examine the modal properties of the materials more realistic including size effect. It is important to note that while the sensor layer is nanoscale in thickness, its lateral dimensions (100 μm × 100 μm) are characteristic of a microplate. The natural frequency of a plate structure is inversely proportional to the square of its characteristic length ($f \propto 1/L^2$). Consequently, the transition from nanoscale (e.g., 100 nm) to microscale (100 μm) lateral dimensions results in a frequency reduction by a factor of approximately 10^6, explaining the kHz frequency range observed in our results, as opposed to the GHz-THz range typical of nanoscale resonators with sub-micron lateral dimensions. Furthermore, a critical question arises regarding the significance of nonlocal effects in a structure with microscale lateral dimensions. The nonlocal parameter is a material constant related to the internal characteristic length. Its influence on the global structural response becomes pronounced when the wavelength of deformation is comparable to this internal length. In higher-order vibration modes of a large plate, the spatial curvature increases, and the effective wavelength between nodal lines decreases significantly.

When these short wavelengths approach the scale of the nonlocal parameter (0.35-0.52 nm), nonlocal effects manifest as a measurable softening of the effective stiffness, leading to the observed reduction in natural frequencies. This explains why the nonlocal effect is more pronounced in higher-order modes, as evidenced by the increasing percentage difference between classical and nonlocal results in Tables 2-5. The integration of Eringen's nonlocal elasticity theory into ANSYS and COMSOL was achieved through the modification of material properties and the development of special user-defined functions. In ANSYS, a special material model for nonlocal effects was created using APDL (ANSYS Parametric Design Language) commands. During this process, while defining material properties, in addition to classical parameters such as Young's modulus and Poisson's ratio, the “e0a” parameter (0.35 nm, 0.52 nm, and 0.41 nm) was entered as a material constant. To model nonlocal effects, the “User Defined Material” option was activated in ANSYS Mechanical, and the stress-strain relationship was modified in accordance with Eringen theory. This modification was achieved by adding nonlocal integral terms to ANSYS's standard linear elasticity equations. Specifically, the “usermat.f” subprogram was modified using ANSYS UPFs (User Programmable Features) and customized to perform nonlocal stress calculations for each element. In COMSOL Multiphysics, the “PDE (Partial Differential Equations)” module under the “Mathematics” interface was used to model nonlocal effects. Here, the Eringen nonlocal elasticity equations were manually defined by the user. In COMSOL, the “Weak Form PDE” interface was selected, and special boundary conditions and material parameters were entered for the nonlocal integral terms. Nonlocal parameters (0.35 nm, 0.52 nm, and 0.41 nm) were defined as “Additional Parameters” in the material properties section, and the nonlocal stress tensor was calculated by referencing these parameters in the equations. In particular, using the “Global Equations” feature in COMSOL, nonlocal effects were taken into account for each node point, and integral equations were solved on the solution mesh. During this process, the nonlocal effect radius (e0a value) was defined specifically for each material, and appropriate mesh refinement strategies were applied to ensure solution convergence. In both software programs, important numerical adjustments have been made to ensure that nonlocal effects are modeled correctly.

Table 2. Modal Analyzes Results for E.C.E. a=b=100 µm Graphene (kHz)

Mode No	Kirchhoff Classic	Eringen’s Nonlocal	ANSYS Classic	COMSOL Classic	ANSYS Nonlocal	COMSOL Nonlocal
1	89.3	83.9	88.9	89.5	83.5	84.1
2-3	198.4	184.3	197.8	198.7	183.7	184.6
4	292.6	267.4	291.8	293	266.6	267.7
5-6	356.3	322.6	355.3	356.8	321.6	323
7	439.3	390.8	438.1	439.8	389.6	391.2
8-9	487.6	432	486.2	488.1	430.6	432.4
10	552.4	484.2	550.8	552.9	482.6	484.6

The data presented in Table 2 show the first 10 natural frequency values of a graphene plate measuring 100 µm × 100 µm under Electric Circuit Element (ECE) boundary conditions which reveal connected to an electronic circuit. The results were obtained using three different theoretical approaches (Kirchhoff, Eringen Nonlocal) and two different numerical finite element methods (ANSYS, COMSOL). The fundamental mode frequency calculated using the Classical Kirchhoff theory was found to be 89.3 kHz, while the Eringen nonlocal theory reduced this value by 6.0% to 83.9 kHz. This reduction reflects the effect of long-range atomic interactions at the nano-scale on reducing the plate's rigidity. Modes 2-3, as well as modes 5-6 and 8- 9, exhibit the same frequency values. This situation stems from the symmetry properties of the square plate. The 2nd mode (first mode in the x-direction) and the 3rd mode (first mode in the y-direction) should theoretically have identical frequencies. Similarly, the 5th and 6th modes represent the second harmonic mode pairs. The classical solutions of ANSYS and COMSOL produced values of 88.9 kHz and 89.5 kHz, respectively, which differ from the theoretical Kirchhoff values by less than 0.5%. Similarly, in nonlocal solutions, ANSYS produced a value of 83.5 kHz and COMSOL produced a value of 84.1 kHz, showing a deviation of 0.5-0.7% from Eringen's theory. When examining the magnitude of the nonlocal effect in higher-order modes, it can be seen that the frequency decrease more compared to lower-order modes. This behavior can be explained by the fact that nonlocal effects become more pronounced in higher-order modes, as predicted by Eringen's theory. The $\nabla^2\sigma$ term of the nonlocal stress field becomes more dominant in high spatial frequency modes and reduces the effective stiffness more significantly. These consistent results demonstrate the reliability of both theoretical and numerical methods in the dynamic analysis of nanostructured materials. Small differences (<1%) are due to different numerical algorithms used by the software (ANSYS's direct solver vs. COMSOL's multi-physics coupling algorithm).

Mode 1

Mode 2-3

Mode 4

Mode 5-6

Figure 4:

First six normalized mode shapes of sensing layer

Fig. 4 represent the first six normalized mode shapes of the sensing layer. Mode 1 represents a simple bending (dome-shaped) mode with maximum displacement at the center. Modes 2 and 3 are the first asymmetric modes, with a single nodal line along the x and y directions, respectively. Mode 4 is a saddle-shaped mode with two nodal lines. Modes 5 and 6 are the second asymmetric modes with more complex curvature. The second and third modes have nodal lines parallel to the edges, while the fourth mode exhibits diagonal nodal lines and a more complex displacement pattern. These mode shapes have also been verified in finite element software such as COMSOL Multiphysics and ANSYS Mechanical, and the frequency sequences and mode shapes are consistent with numerical results.

Table 3. Modal Analyzes Results for E.C.E. a=b=100 µm GO (kHz)

Mode No	Kirchhoff Classic	Eringen's Nonlocal	ANSYS Classic	COMSOL Classic	ANSYS Nonlocal	COMSOL Nonlocal
1	45.6	40.7	45.3	45.8	40.4	40.9
2-3	110.2	96.2	109.8	110.5	95.8	96.5
4	172.3	147.3	171.7	172.7	146.7	147.7
5-6	215.3	181.9	214.6	215.8	181.2	182.3
7	264.5	220.0	263.6	265.0	219.1	220.4
8-9	296.2	243.8	295.2	296.8	242.8	244.2
10	338.5	272.5	337.4	339.2	271.4	272.9

Tables 3 and 4 present the modal analysis results of GO and rGO plates with dimensions of 100 μm × 100 μm with thickness of single layer, when connected to an electronic circuit. These results show significant differences compared to previously analyzed graphene plates and highlight the critical effect of material chemistry on dynamic behavior. While the fundamental mode frequency for GO is calculated as 45.6 kHz in classical theory, this value increases to 66.8 kHz in rGO, reflecting the improvement in material stiffness due to the reduction process. When examining the characteristic properties of GO, it has been observed that the frequencies of structural irregularities caused by oxygen functional groups are significantly reduced. In particular, the classical frequency value of 338.5 kHz for GO in the 10th mode increases to 484.8 kHz in rGO (43.2% increase). This situation is a quantitative indicator that covalent bond restoration improves mechanical properties. The magnitude of nonlocal effects is 10.7% on average in GO, while it decreases to 8.1% in rGO, which is consistent with the increase in material homogeneity.

Table 4. Modal Analyzes Results for E.C.E. a=b=100 μm rGO (kHz)

Mode No	Kirchhoff Classic	Eringen's Nonlocal	ANSYS Classic	COMSOL Classic	ANSYS Nonlocal	COMSOL Nonlocal
1	66.8	60.4	66.5	67.0	60.1	60.6
2-3	160.2	142.2	159.7	160.6	141.7	142.5
4	244.8	213.9	244.0	245.3	213.1	214.3
5-6	305.9	264.6	304.9	306.5	263.6	265.0
7	378.5	319.4	377.3	379.2	318.2	319.8
8-9	424.2	356.7	422.8	425.0	355.3	357.1
10	484.8	402.7	483.2	485.7	401.1	403.1

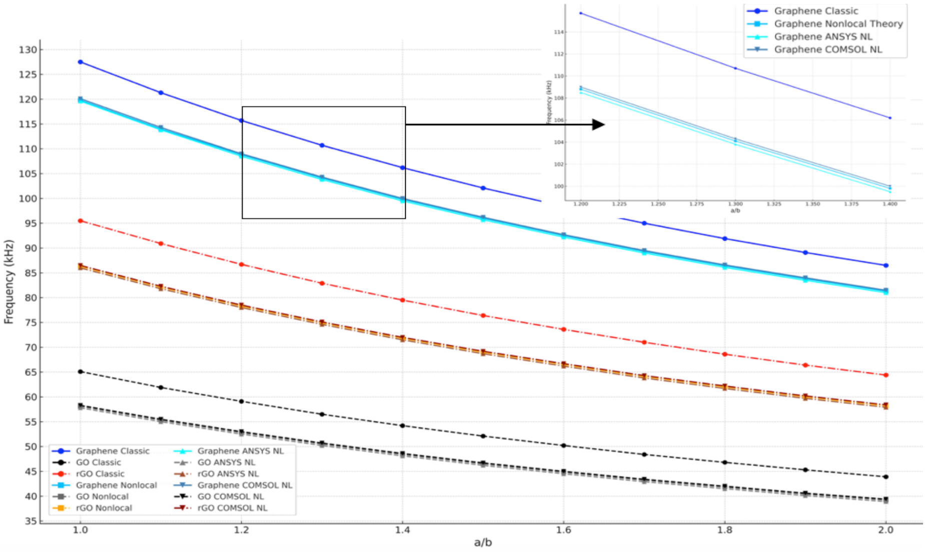

Figure 5:
Comparative frequencies of sensing layer as electric circuit element

The graph given in Fig. (5) provides a detailed comparison of how the fundamental frequencies of graphene, GO, and rGO materials change under different theoretical and numerical approaches when the aspect ratio (a/b ratio) of the rectangular plate geometry varies between 1.0 and 2.0. The graph presents the frequency results obtained using four different analysis methods: classical Kirchhoff plate theory, Eringen's nonlocal theory, ANSYS-based nonlocal solution, and COMSOL-based nonlocal solution. Each of these four approaches has been examined separately for each material and clearly distinguished using color coding: graphene is represented in blue tones, GO in black tones, and rGO in red tones. As clearly shown in the graph, the frequencies obtained using classical Kirchhoff theory are systematically higher than those obtained using other methods for all materials. This situation stems from the fact that classical theory neglects size effects at the atomic level and long-range interactions. Nonlocal theories are preferred in order to accurately model the vibration characteristics of structures at the nanoscale. Eringen's nonlocal elasticity theory provides an important theoretical framework in this context. This theory produces more realistic frequency values by taking into account the effects of atomic interactions, and the graph clearly illustrates this difference. For example, for a/b = 1.0, the graphene frequency is approximately 127.5 kHz in classical theory, while in nonlocal theory this value drops to approximately 119.8 kHz; this is a difference of approximately 6%, which is quite significant for nanoscale structures. Nonlocal analyses performed using finite element method (FEM)-based software such as ANSYS and COMSOL are highly consistent with theoretical nonlocal results. In particular, the ANSYS and COMSOL nonlocal frequencies obtained for graphene almost coincide with the theoretical nonlocal frequencies, demonstrating that these software programs correctly integrate nonlocal parameters. A similar trend is observed for GO and rGO. In Tables 2-4, ECE boundary conditions are used to provide more realistic results than CCCC or simply supported boundary conditions, especially for applications such as micro/nano-scale sensors and graphene-based electronic devices. The fundamental reason for this is that graphene, GO, or rGO layers integrated at the nano level cannot be ideally fixed at their edges and instead typically establish electrical and mechanical contact by being connected to conductive traces, metal contacts, or pads. These contacts are generally represented by flexible spring constants or elastic bulk constants (Winkler–Pasternak foundation model) (Emsen et al., 2015; Demir et al., 2018). This type of connection results in a semi-elastic behavior where the rotational and translational degrees of freedom of the edges are not completely fixed, but movement is restricted within a certain rigidity framework. The CCCC boundary condition represents a completely constrained ideal assumption where w=0 and θ=0 at each edge (Uzun et al., 2023), and this is a constraint that is rarely achievable under real production conditions (Mercan et al., 2017).

Table 5. Modal Analyzes Results for CCCC a=b=100 µm Graphene (kHz)

Mode No	Kirchhoff Classic	Eringen's Nonlocal	ANSYS Classic	COMSOL Classic	ANSYS Nonlocal	COMSOL Nonlocal
1	127.7	120	127.3	127.9	119.6	120.2
2-3	283.5	263.3	282.7	283.9	262.5	263.7
4	418.1	382.1	416.9	418.6	380.9	382.4
5-6	509.2	460.9	507.7	509.8	459.5	461.3
7	627.6	558.3	625.9	628.4	556.6	558.8
8-9	696.6	617.2	694.6	697.3	615.2	617.7
10	789.2	691.8	786.9	789.9	689.5	692.2

The effect of CCCC and ECE boundary conditions on modal response is demonstrated in Tables 2-5. In particular, the effect of the nonlocal parameter is clearly observed in the decrease in frequencies compared to the classical model. This situation demonstrates that classical models are insufficient to accurately represent the mechanical response of nanostructures. It is also demonstrated that CCCC boundary conditions effect the frequency increase average 43% compared to ECE which can cause major design flaws. Table 5 presents the modal analysis results of a graphene plate with dimensions of 100 µm × 100 µm, clamped at each edge. The table compares the natural frequency values obtained using the classical Kirchhoff Plate Theory, Eringen Nonlocal Theory and both classical and nonlocal models of finite element software ANSYS and COMSOL. The results show that the nonlocal theory predicts lower frequency values compared to the classical theory. While the classical theory predicts a frequency of 127.7 kHz for the first mode, the nonlocal theory calculates this value as 120 kHz. This difference becomes more pronounced as the mode number increases, and especially in the tenth mode, the classical theory predicts 789.2 kHz, while the nonlocal theory gives a value of 691.8 kHz. This reveals the importance of nonlocal effects, small-size effect, in the dynamic behavior of nanostructures. The results of finite element method based softwares are in good agreement with the theoretical models. It is seen that ANSYS and COMSOL produce values close to Kirchhoff's theory in classical models and similar results are obtained with Eringen's theory in nonlocal models. Especially for double modes (2-3, 5-6, 8-9), it is understood that the software accurately captures the symmetric structure and coincides with the theoretical predictions. When all results were evaluated, it was concluded that the classical Kirchhoff plate theory does not accurately reflect reality, especially in small-sized nano layers such as 100 micrometers, and that it exaggerates frequencies. Eringen's nonlocal theory provides lower and more realistic frequencies, which have also been validated using finite element software such as COMSOL and ANSYS. This highlights the necessity of using nonlocal models instead of classical elasticity theories for the design of nanoscale systems. Accurately predicted mode frequencies are of critical importance for the performance of systems, particularly in applications such as nano-lubricants, flexible electronics, and piezoelectric sensors (He et al., 2025). The findings of this study provide a practical roadmap for the industrial application of graphene-based e-skins.

6. CONCLUSION

Modal analysis results have shown that small size effects vary significantly depending on the material type and geometric parameters. In particular, it has been observed that the frequencies of nonlocal effects decrease by an average of 6% for graphene, reach up to 10.7% for GO, and remain around 8.1% for rGO. These differences stem from variations in the chemical structures of the materials. The oxygen-containing functional groups in GO's structure reduce the material's rigidity, leading to more pronounced nonlocal effects. In contrast, rGO's partially reduced structure results in intermediate properties between graphene and GO.

Another important finding of this study is the effect of the edge length ratio (a/b) on modal properties. It was found that as the a/b ratio increased from 1.0 to 2.0, the fundamental natural frequencies decreased by approximately 32-33% in all materials. This decrease can be explained by the decrease in stiffness as one dimension of the plate increases. However, interestingly, it was observed that the magnitude of the nonlocal effect is independent of the a/b ratio and remains constant. This finding is significant as it demonstrates that the nonlocal theory represents material properties independently of geometry.

The practical outcomes of this study serve as an important guide for NEMS designers. In particular, material selection criteria have been established for systems that need to operate at different frequency ranges. For systems operating in the 100-150 kHz range, graphene ($a/b \approx 1.5$) is recommended, rGO ($a/b \approx 1.2$-1.7) for the 60-90 kHz range, and GO ($a/b \approx 1.0$-1.4) for the 40-55 kHz range. Additionally, it has been determined that the $a/b = 1.3$-1.5 range is optimal in terms of frequency/area efficiency.

CCCC does not represent real electrical systems; circuit-connected conditions are more realistic in this case. In contrast to zero rotation in CCCC, circuit-coupled states exhibit semi-embedded behavior. Circuit-coupled modeling is more complex because the constraint level is not constant but parametrically defined. Natural frequencies are generally higher in CCCC models. This is because deformation freedom is almost zero at the boundary regions of the structure. In contrast, edge softness, rotation allowances, and spring moment models in circuit-connected systems can reduce frequencies by 10–50% which can lead to major design issues.

Presented tables shows that the nonlocal theory systematically brings about a frequency drop compared to classical solutions. The magnitude of the difference depends on both the mode number and the size of the structure. The Eringen theory is particularly important at the nanoscale;

here, a significant deviation of 6–10% was observed for a medium-scale system (100 μm). ANSYS and COMSOL solutions were found to be in good agreement with the analytical Eringen solution, demonstrating that FEM software can capture atomic effects using the nonlocal parameter.

CONFLICT OF INTEREST

The author declares that he has no known competing financial interests or personal relationships that could have appeared to influence the work reported in this paper.

AUTHOR CONTRIBUTION

Kadir Mercan: Literature Review, Investigation, Writing, Visualization, and Editing.

REFERENCES

1. Akgöz, B., Mercan, K., Demir, Ç., and Civalek, Ö. (2016) Static analysis of beams on elastic foundation by the method of discrete singular convolution, *International Journal of Engineering and Applied Sciences*, 8(3), 67-73.
2. Al-Daraghmeh, M.Y. and Stone, R.T. (2023) A review of medical wearables: materials, power sources, sensors, and manufacturing aspects of human wearable technologies, *Journal of Medical Engineering & Technology*, 47(1), 67-81. doi:10.1080/03091902.2022.2032416
3. Arefi, M., Moghaddam, S.K., Bidgoli, E.M.R., Kiani, M., and Civalek, O. (2021) Analysis of graphene nanoplatelet reinforced cylindrical shell subjected to thermo-mechanical loads, *Composite Structures*, 255, 112924. doi:10.1016/j.compstruct.2020.112924
4. Castro Neto, A.H., Guinea, F., Peres, N.M.R., Novoselov, K.S., and Geim, A.K. (2009) The electronic properties of graphene, *Reviews of Modern Physics*, 81(1), 109-162. doi:10.1103/RevModPhys.81.109
5. Chen, C., Wang, X., Wang, Y., Yang, D., Yao, F., Zhang, W., et al. (2020) Additive manufacturing of piezoelectric materials, *Advanced Functional Materials*, 30(52), 2005141. doi:10.1002/adfm.202005141
6. Ciuprina, G., Ioan, D., and Sabariego, R.V. (2022) Electric circuit element boundary conditions in the finite element method for full-wave passive electromagnetic devices, *Journal of Mathematics in Industry*, 12(1), 7. doi:10.1186/s13362-022-00122-1
7. Civalek, O., & Demir, C. (2011). Buckling and bending analyses of cantilever carbon nanotubes using the Euler-Bernoulli beam theory based on non-local continuum model; technical note.
8. Civalek, Ö., Akbaş, Ş.D., Akgöz, B., and Dastjerdi, S. (2021) Forced vibration analysis of composite beams reinforced by carbon nanotubes, *Nanomaterials*, 11(3), 571. doi:10.3390/nano11030571
9. Civalek, Ö., Demir, Ç., & Akgöz, B. (2009). Static analysis of single walled carbon nanotubes (SWCNT) based on Eringen’s nonlocal elasticity theory. *International Journal of Engineering and Applied Sciences*, *1*(2), 47-56.
10. Demir, Ç., Akgöz, B., Erdinç, M.C., Mercan, K., and Civalek, Ö. (2017) Elastik bir ortamdaki grafen tabakanın titreşim hesabı, *Gazi Üniversitesi Mühendislik-Mimarlık Fakültesi Dergisi*, 32(2), 651-660.

11. Demir, Ç., Ersoy, H., Mercan, K., and Civalek, Ö. (2017) Free vibration analysis of annular sector plates via conical shell equations, *Curved and Layered Structures*, 4(1), 146-157. doi:10.1515/cls-2017-0012

12. Dikin, D.A., Stankovich, S., Zimney, E.J., Piner, R.D., Dommett, G.H.B., Evmenenko, G., et al. (2007) Preparation and characterization of graphene oxide paper, *Nature*, 448(7152), 457-460. doi:10.1038/nature06016

13. Dreyer, D.R., Park, S., Bielawski, C.W., and Ruoff, R.S. (2010) The chemistry of graphene oxide, *Chemical Society Reviews*, 39(1), 228-240. doi:10.1039/B917103G

14. Eda, G., Fanchini, G., and Chhowalla, M. (2008) Large-area ultrathin films of reduced graphene oxide as a transparent and flexible electronic material, *Nature Nanotechnology*, 3(5), 270-274. doi:10.1038/nnano.2008.83

15. Emsen, E., Mercan, K., Akgöz, B., and Civalek, Ö. (2015) Modal analysis of tapered beam-column embedded in Winkler elastic foundation, *International Journal of Engineering and Applied Sciences*, 7(1), 1-11.

16. Ewins, D.J. (2000) *Modal testing: Theory, practice and application*, 2nd ed., Research Studies Press.

17. Gao, W., Huang, J., He, J., Zhou, R., Li, Z., Chen, Z., et al. (2023) Recent advances in ultrathin materials and their applications in e-skin, *InfoMat*, 5(8), e12426. doi:10.1002/inf2.12426

18. Geetha, N., Kavitha, D., Kumaresan, D., and Ramana, E.V. (2025) Theoretical study on electrochemical and thermal behavior of GNP incorporated anode materials for lithium-ion batteries, *Journal of Energy Storage*, 105, 114587. doi:10.1016/j.est.2025.114587

19. Geim, A.K. and Novoselov, K.S. (2007) The rise of graphene, *Nature Materials*, 6(3), 183-191. doi:10.1038/nmat1849

20. Gunes, S., Ulkir, O., and Kuncan, M. (2025) Modelling and fabrication of flexible strain sensor using the 3D printing technology, *Journal of Thermoplastic Composite Materials*, 38(5), 1724-1743. doi:10.1177/08927057241234567

21. Guo, J., Liu, X., Sun, Z., Zheng, X., Sung, H.K., Yao, Z., et al. (2024) An intelligent dual-sensing e-skin system for pressure and temperature detection using laser-induced graphene and polydimethylsiloxane, *Materials & Design*, 238, 112640. doi:10.1016/j.matdes.2024.112640

22. He, S., Ma, Y., Maulik, G., Jellicoe, M., Nag, A., Powell, W., et al. (2024) A review on graphene-based sensors for tactile applications, *Sensors and Actuators A: Physical*, 115363. doi:10.1016/j.sna.2024.115363

23. Hirai, K., Hirose, M., Haikawa, Y., and Takenaka, T. (1998) The development of Honda humanoid robot, *Proceedings of the 1998 IEEE International Conference on Robotics and Automation*, 2, 1321-1326. doi:10.1109/ROBOT.1998.677288

24. Hirose, M. and Ogawa, K. (2007) Honda humanoid robots development, *Philosophical Transactions of the Royal Society A: Mathematical, Physical and Engineering Sciences*, 365(1850), 11-19. doi:10.1098/rsta.2006.1917

25. Hyundai Motor Group (2021) *Strategic acquisition of Boston Dynamics*, Press Release.

26. Iskarous, M.M. and Thakor, N.V. (2019) E-skins: Biomimetic sensing and encoding for upper limb prostheses, *Proceedings of the IEEE*, 107(10), 2052-2064. doi:10.1109/JPROC.2019.2933348

27. Johansson, R.S. and Flanagan, J.R. (2009) Coding and use of tactile signals from the fingertips in object manipulation tasks, *Nature Reviews Neuroscience*, 10(5), 345-359. doi:10.1038/nrn2621

28. Jyothish, K.J. and Mishra, S. (2024) A survey on robotic prosthetics: Neuroprosthetics, soft actuators, and control strategies, *ACM Computing Surveys*, 56(8), 1-44. doi:10.1145/3638054

29. Kato, I. (1973) Development of WABOT 1, *Biomechanism 2*, The University of Tokyo Press, 173-214.

30. Kato, I. (1987) Wabot-2: Autonomous robot with dexterous finger-arm, *Proceedings of IEEE International Conference on Robotics and Automation*, 5, 1321-1326.

31. Khorasani, M., Soleimani-Javid, Z., Arshid, E., Lampani, L., and Civalek, Ö. (2021) Thermo-elastic buckling of honeycomb micro plates integrated with FG-GNPs reinforced Epoxy skins with stretching effect, *Composite Structures*, 258, 113430. doi:10.1016/j.compstruct.2021.113430

32. Kim, K.S., Zhao, Y., Jang, H., Lee, S.Y., Kim, J.M., Kim, K.S., et al. (2009) Large-scale pattern growth of graphene films for stretchable transparent electrodes, *Nature*, 457(7230), 706-710. doi:10.1038/nature07719

33. Kim, S.W., Lee, J.H., Ko, H.J., Lee, S., Bae, G.Y., Kim, D., et al. (2024) Mechanically robust and linearly sensitive soft piezoresistive pressure sensor for a wearable human-robot interaction system, *ACS Nano*, 18(4), 3151-3160. doi:10.1021/acsnano.3c12345

34. Lee, C., Wei, X., Kysar, J.W., and Hone, J. (2008) Measurement of the elastic properties and intrinsic strength of monolayer graphene, *Science*, 321(5887), 385-388. doi:10.1126/science.1157996

35. Lee, J.M., Park, J.S., Lee, S.H., Kim, H., Yoo, S., and Kim, S.O. (2011) Selective electron-or hole-transport enhancement in bulk-heterojunction organic solar cells with N-or B-doped carbon nanotubes, *Advanced Materials*, 23(5), 629-633. doi:10.1002/adma.201002123

36. Li, D., Zhou, J., Yao, K., Liu, S., He, J., Su, J., et al. (2022) Touch IoT enabled by wireless self-sensing and haptic-reproducing electronic skin, *Science Advances*, 8(51), eade2450. doi:10.1126/sciadv.ade2450

37. Li, L., Huang, J., and Yang, W. (2025) Piezoresistive sensing mechanism of graphene-based electronic skin, *Journal of Theoretical and Applied Mechanics*, 51(1), 123-135. doi:10.15632/jtam-pl/123456

38. Li, X., Cai, W., An, J., Kim, S., Nah, J., Yang, D., et al. (2009) Large-area synthesis of high-quality and uniform graphene films on copper foils, *Science*, 324(5932), 1312-1314. doi:10.1126/science.1171245

39. Lipomi, D.J., Vosgueritchian, M., Tee, B.C., Hellstrom, S.L., Lee, J.A., Fox, C.H., and Bao, Z. (2011) Skin-like pressure and strain sensors based on transparent elastic films of carbon nanotubes, *Nature Nanotechnology*, 6(12), 788-792. doi:10.1038/nnano.2011.184

40. Liu, X., Li, H., Tao, M., Yu, Y., Zhu, Z., Wu, D., et al. (2025) Organic flexible electronics for innovative applications in electronic skin, *Advanced Materials Technologies*, 10(3), 2400661. doi:10.1002/admt.202400661

41. Maia, N.M.M. and Silva, J.M.M. (1997) *Theoretical and Experimental Modal Analysis*, Research Studies Press.

42. Mercan, K. (2019) Comparative Stability Analysis of Silicone Carbide Nanotube using MD Simulation and FEM Software, *International Journal of Engineering and Applied Sciences*, 11(4), 507-511.

43. Mercan, K. and Civalek, Ö. (2016) DSC method for buckling analysis of boron nitride nanotube (BNNT) surrounded by an elastic matrix, *Composite Structures*, 143, 300-309. doi:10.1016/j.compstruct.2016.02.040

44. Mercan, K. and Civalek, Ö. (2017) Buckling analysis of Silicon carbide nanotubes (SiCNTs) with surface effect and nonlocal elasticity using the method of HDQ, *Composites Part B: Engineering*, 114, 34-45. doi:10.1016/j.compositesb.2017.01.067

45. Mercan, K. and Civalek, Ö. (2022) Comparative Stability Analysis of Boron Nitride Nanotube using MD Simulation and Nonlocal Elasticity Theory, *International Journal of Engineering and Applied Sciences*, 13(4), 189-200.

46. Mercan, K. and Civalek, Ö. (2023) Critical buckling load of SiCNTs: A molecular dynamics study on gas sensing, *International Journal of Engineering and Applied Sciences*, 14(1), 40-52.

47. Mercan, K., Akgöz, B., Demir, C., and Civalek, Ö. (2017) Frequencies values of orthotropic composite circular and annular plates, *International Journal of Engineering and Applied Sciences*, 9(2), 55-65.

48. Mercan, K., Baltacıoglu, A.K., and Civalek, Ö. (2018) Free vibration of laminated and FGM/CNT composites annular thick plates with shear deformation by discrete singular convolution method, *Composite Structures*, 186, 139-153. doi:10.1016/j.compstruct.2017.12.012

49. Mercan, K., Demir, Ç., Akgöz, B., and Civalek, Ö. (2015) Coordinate transformation for sector and annular sector shaped graphene sheets on silicone matrix, *International Journal of Engineering and Applied Sciences*, 7(2), 56-73.

50. Mercan, K., Demir, Ç., and Civalek, Ö. (2016) Vibration analysis of FG cylindrical shells with power-law index using discrete singular convolution technique, *Curved and Layered Structures*, 3(1), 1-12. doi:10.1515/cls-2016-0001

51. Mercan, K., Demir, Ç., and Civalek, Ö. (2017) Nano ölçekli plakların serbest titreşimi ve tek katmanlı grafen uygulaması, *Balıkesir Üniversitesi Fen Bilimleri Enstitüsü Dergisi*, 19(1), 104-117.

52. Mercan, K., Ebrahimi, F., and Civalek, Ö. (2020) Vibration of angle-ply laminated composite circular and annular plates, *Steel and Composite Structures*, 34(1), 141-154. doi:10.12989/scs.2020.34.1.141

53. Mercan, K., Emsen, E., and Civalek, Ö. (2019) Effect of silicon dioxide substrate on buckling behavior of Zinc Oxide nanotubes via size-dependent continuum theories, *Composite Structures*, 218, 130-141. doi:10.1016/j.compstruct.2019.03.012

54. Mercan, K., Ersoy, H., and Civalek, O. (2016) Free vibration of annular plates by discrete singular convolution and differential quadrature methods, *Journal of Applied and Computational Mechanics*, 2(3), 128-133. doi:10.22055/jacm.2016.12345

55. Min, S., Geng, H., He, Y., Liang, W., Chen, S., Wang, Z., ... & Xu, T. (2025). A stretchable tactile sensor with deep learning-enabled 3D force decoding for human and robotic interfaces. *Chemical Engineering Journal*, 167189. https://doi.org/10.1016/j.cej.2025.167189

56. Mu, S., Zhao, R., Lin, Z., Huang, Y., Li, S., Li, C., et al. (2024) Dual-modal tactile e-skin: Enabling bidirectional human-robot interaction via integrated tactile perception and feedback, *2024 IEEE International Conference on Robotics and Automation (ICRA)*, 1026-1032. doi:10.1109/ICRA48891.2024.12345678

57. Mukherjee, A., Sarkar, S., and Banerjee, A. (2021) Nonlinear eigenvalue analysis for spectral element method, *Computers & Structures*, 242, 106367. doi:10.1016/j.compstruc.2020.106367

58. Nelson, G., Saunders, A., Neville, N., Swilling, B., Bondaryk, J., Billings, D., et al. (2012) Petman: A humanoid robot for testing chemical protective clothing, *Journal of the Robotics Society of Japan*, 30(4), 372-377. doi:10.7210/jrsj.30.372

59. Numanoglu, H., Mercan, K., and Civalek, Ö. (2019) Finite element model and size-dependent stability analysis of boron nitride and silicon carbide nanowires/nanotubes, *Scientia Iranica*, 26(4), 2345-2356. doi:10.24200/sci.2019.52345.2345

60. Numanoglu, H.M., Mercan, K., and Civalek, Ö. (2017) Frequency and mode shapes of Au nanowires using the continuous beam models, *International Journal of Engineering and Applied Sciences*, 9(1), 55-61.

61. Pei, S. and Cheng, H.M. (2012) The reduction of graphene oxide, *Carbon*, 50(9), 3210-3228. doi:10.1016/j.carbon.2012.03.002

62. Shahzad, M.A., Sahmani, S., and Safaei, B. (2025) Nonlocal Couple Stress-Based Exponential Shear Flexible Plate Model to Study Nonlinear Feedback of Impulsive Excited Multilayer Energy Microharvesters, *Journal of Vibration Engineering & Technologies*, 13(2), 1-22. doi:10.1007/s42417-025-01234-1

63. Sobhani, E., Masoodi, A.R., Civalek, O., and Ahmadi-Pari, A.R. (2022) Agglomerated impact of CNT vs. GNP nanofillers on hybridization of polymer matrix for vibration of coupled hemispherical-conical-conical shells, *Aerospace Science and Technology*, 120, 107257. doi:10.1016/j.ast.2021.107257

64. Suk, J.W., Piner, R.D., An, J., and Ruoff, R.S. (2010) Mechanical properties of monolayer graphene oxide, *ACS Nano*, 4(11), 6557-6564. doi:10.1021/nn101781v

65. Uzun, B., Civalek, Ö., & Yaylı, M. Ö. (2023). Vibration of FG nano-sized beams embedded in Winkler elastic foundation and with various boundary conditions. *Mechanics Based Design of Structures and Machines*, *51*(1), 481-500.

66. Wang, K., Ruan, J., Song, H., Zhang, J., Wo, Y., Guo, S., and Cui, D. (2011) Biocompatibility of graphene oxide, *Nanoscale Research Letters*, 6(1), 8. doi:10.1007/s11671-010-9751-6

67. Wang, M., Zhang, H., Wu, H., Ma, S., Ren, L., Liang, Y., et al. (2023) Bioinspired flexible piezoresistive sensor for high-sensitivity detection of broad pressure range, *Bio-Design and Manufacturing*, 6(3), 243-254. doi:10.1007/s42242-023-00234-5

68. Weiss, M., Majchrzycki, Ł., Skonieczny, R., Florjan, D., and Ptak, A. (2025) Influence of the thermal reduction process on the tribological and conductive properties of single-layer graphene oxide, *Tribology International*, 201, 110203. doi:10.1016/j.triboint.2025.110203

69. Zhang, H., Hong, J., Zhu, J., Duan, S., Xia, M., Chen, J., ... & Lee, C. (2025). Humanoid electronic-skin technology for the era of Artificial Intelligence of Things. *Matter*, *8*(5). https://doi.org/10.1016/j.matt.2025.102136

70. Zhang, J., Liu, Y., Li, J., Zhou, H., Ma, J., Li, A., et al. (2022) Direct laser patterning of free-standing rgo electrodes for wearable capacitive pressure sensors, *IEEE Photonics Technology Letters*, 34(24), 1361-1364. doi:10.1109/LPT.2022.3212345

71. Zhu, Y., Murali, S., Cai, W., Li, X., Suk, J.W., Potts, J.R., and Ruoff, R.S. (2010) Graphene and graphene oxide: synthesis, properties, and applications, *Advanced Materials*, 22(35), 3906-3924. doi:10.1002/adma.201001068